Synthesis of Microporous Nano-Composite (Hollow Spheres) for Fast Detection and Removal of As(V) from Contaminated Water

Osama Zaid, Waleed El-Said, Ahmed Yousif, Ahmed Galhoum, Emad Elshehy, Ibrahim Ibrahim, Eric Guibal

Synthesis of microporous nano-composite (hollow spheres) for fast detection and removal of As(V) from contaminated water

Osama F. Zaid[a], Waleed A. El-Said[b,c], Ahmed M. Yousif[a,d], Ahmed A. Galhoum[e,*], Emad A. Elshehy[e,*], Ibrahim A. Ibrahim[f], Eric Guibal[g,*]

[a] Chemistry Department, Faculty of Science, Menoufia University, Shebin El-Kom, Menoufia, Egypt
[b] Chemistry Department, Faculty of Science, Assiut University, Assiut, Egypt
[c] University of Jeddah, College of Science, Department of Chemistry, P.O. 80327, Jeddah 21589, Saudi Arabia
[d] Chemistry Department, College of Science and Arts, Jouf University, Alqurayyat, Saudi Arabia
[e] Nuclear Materials Authority, P.O. Box 530, El-Maadi, Cairo, Egypt
[f] Central Metallurgical Research & Development Institute (CMRDI), Helwan 11421, Egypt
[g] Polymers Composites Hybrids (PCH) IMT Mines Ales, 6 Avenue de Clavières, F-30319 Alès cedex, France

HIGHLIGHTS

- Simple synthesis of hollow–wagon-wheel sorbent (with CA/CTAB sacrificed template).
- High surface-area microporous hollow spheres of silica@Mo(VI) for As(V) sorption.
- Pseudo-first order rate and Sips equations for modeling kinetics and isotherms.
- Used as naked-eye sensor, the material detects As(V) at level as low as 0.3 μM.
- Efficient As(V) desorption using 1 mM NaOH solution and high recycling performance.

ABSTRACT

A simple method has been designed for preparing a new material based on the interactions of cellulose acetate (mixed with an alkaline urea solution, CA/urea), cetyltrimethylammonium bromide (CTAB) with tetraethyl orthosilicate in alcohol (CTAB/TEOS). In a second step, the material is loaded with molybdate. The nano-objects produced by this procedure are characterized as microporous hollow spheres with a morphology similar to hollow wagon-wheels. These materials were used not only for As(V) removal (specific affinity of As(V) for Mo (VI)), but also for naked-eye detection of As(V) in solution. The chemical and physical characteristics of these nano-objects have been analyzed through XRD, FTIR, HR-TEM, EDX, TGA/DTG and N_2 sorption/desorption isotherms. The nano-sized sorbent/sensor has large surface-to-volume ratios (715.5 $m^2\ g^{-1}$ and 0.295 $cm^3\ g^{-1}$, respectively). Sorption capacity reaches 2 mmol As g^{-1} at optimum pH 1.8. Fast mass transfer properties allows reaching the equilibrium within 20–25 min (kinetics controlled by pseudo-first order rate equation). This structure allows ultra-fast, specific and pH-dependent visual detection of As(V): the limit of detection is evaluated to 0.3 μmol L^{-1} (limit of quantification: ≈1 μmol L^{-1}). The nano-particles show remarkable long-term stability with good reproducibility after five regeneration cycles (loss in sorption and desorption efficiencies less than 5%). The recovery of As(V) from dilute solutions reaches up to 93%, when applied to water collected from Nile river.

Keywords:
Arsenic removal
Core-shell nanoparticles
Sensors
Silica
Molybdenum oxide
Water treatment

1. Introduction

The strong impact of inorganic contaminants on human health and biotope, through possible carcinogenic, mutagenic and toxic effects, may explain the drastic policies on industrial wastewater but also the development of treatment processes to fit the regulations for drinking water, feedstock and irrigation uses [1–5]. Arsenate is the highest noxious among inorganic hazardous substances, as reported by WHO and EPA organizations [5–9]. Arsenic is highly persistent in water bodies and aquifers (being present under different forms as inorganic As

* Corresponding authors.
E-mail addresses: Galhoum_nma@yahoo.com (A.A. Galhoum), eelshehy@yahoo.com (E.A. Elshehy), Eric.Guibal@mines-ales.fr (E. Guibal).

(V) and As(III) or as organoarsenate species), combined to bioaccumulation effects in the food chain, this contaminant represents an important threat for human beings and animals. People exposed to chronic arsenic contamination may develop cancers (especially to liver, lung, kidney, prostate, bladder and gastrointestinal organs) in addition to nerve tissue injuries, hard patches and skin pigmentation [10–13]. Trace levels of arsenite/arsenate are of special concern because of their high irreversible damage to human cells. This worldwide problem affects over millions of humans due to naturogenic sources and anthropogenic causes, such as refining petroleum and waste streams from mineral processing [7,14–17]. Arsenic is also widespread in Egypt, occurring in phosphate mineral and various other mineral deposits with an average of 0.95 ppm [18,19]. In 2001, USEPA and WHO recommended the decrease of maximum allowable limit for As in drinking water to 10 ppb [14,15,17].

Several methods have been investigated for the removal of As from contaminated water such as adsorption, co-precipitation, nano-filtration, coagulation, cementation or electrodialysis treatment techniques [18–24]. Sorption processes show many advantages associated with fine selectivity, low cost, limited energy requirements (compared with membrane processes) and limited production of sub-products and sludge (compared with precipitation, coagulation-flocculation). They can be also used as pre-concentration steps in analytical processes [25]. Different adsorbents such as metal oxides, activated carbons, resins, impregnated resins [26], metal-organic frameworks (MOFs) [27], nanocomposites and biosorbents have been reported for As removal [11,28–34]. Cellulose support modified with grafting of amine groups has been used for the binding of copper and the metal-loaded sorbent was efficiently used for As(V) recovery [35–38]. Molybdate ions are well known for their affinity for arsenate and this interaction has been reported for developing analytical methods but also molybdate-impregnated sorbents that are highly efficient for As(V) recovery [39,40]. The incorporation of Mo(VI) ions in a polymer composite (Silica/CA-CTAB) (associating silica and cellulose acetate (CA) treated with cetyl trimethyl ammonium bromide (CTAB)) opens possibility for the support to bind metal anions such as arsenate. This synthesis procedure allows preparing new nano-spherical core/shell nanoparticles of SiO_2@Mo(VI) assembled in a wagon-wheel shape. This is a new way to synthesize a microporous sorbent with an ultra-thin inorganic top layer of molybdate anions on silica surface. Silica particles incorporated with other metal oxides show excellent thermal and mechanical stabilities, cost-effective, nontoxic nature with relatively simple fabrication methods and high adsorption capacities [41–46].

The study focuses on the evaluation of the sorption properties of this new material for As(V) removal from aqueous solutions. However, this material can be also used as a sensor; making profit of (a) the interaction of the support for molybdate and arsenic, (b) the specific morphology and pore connectivity of the composite material, and (c) the color change of the sorbent after As(V) binding through formation of hydrogen bonds, electrostatic interactions and/or ion-pair complexation. The color change can be enhanced by reaction with ascorbic acid, which involves a change in the oxidation state of metal species (especially molybdate) [47,48].

Many laboratory techniques were developed for detection and quantification of arsenic at trace levels, including atomic absorption hydride generation and emission spectrometry (HG-AAS/AES), organic fluorophore based assays and high-performance liquid chromatography (HPLC) [49–55]. Despite their high sensibility, these technologies might not be suitable for periodical field analysis because of the use of costly, complex and/or time-consuming instruments. Therefore, new approaches are of strategic importance for making available cost-effective, readily operable as well as highly sensitive methods and materials for the detection and quantification of toxic species, such as As (V), in water samples.

Furthermore, the complex formed between Silica/CA-CTAB@MoO and As(V) changes its color in the presence of a small amount of reducing agent such as ascorbic acid. Spectrophotometric measurements of the solution containing the fabricated optical microporous sensor (in ascorbate-containing media) may be used for precise quantification of arsenic traces. The study explores the impact of parameters such as pH, contact time, temperature, arsenic concentration, presence of co-existing ions on the sorption of As(V) but also on the analytical potential of this new material (after ascorbic conditioning). The work also investigates the re-use of the sorbent for a series of cycles of sorption and desorption.

Thus, synthesized composite is a highly promising candidate for elaborating optical sensor: its unique morphology, self-functionalized surface, and physical properties enhance the sensitivity, selectivity, and time-response of the sensor. The key result in this study is the ion-selective determination of arsenic in real matrix (Nile water) of the optical meso-captor, based on the porous structure of SiO_2@Mo(VI)-HS.

2. Materials and methods

2.1. Materials

All materials were used as received with analytical grade and without further purification. Tetraethyl orthosilicate (TEOS, 99.9%), cetyltrimethylammonium bromide (CTAB, 98%), cellulose acetate powder (CA), ammonium molybdate tetrahydrate [$(NH_4)_6Mo_7O_{24}{\cdot}4H_2O$], urea (98%), ammonium hydroxide, (33% NH_3), ethylenediaminetetraacetic acid (EDTA), NaOH, $CuCl_2$, $Fe(NO_3)_3$, $MnCl_2$, $PbCl_2$, Na_2SO_4, $MgSO_4$, $CaCl_2$, $NiCl_2$, $CoBr_2$, $Hg(NO_3)_2$, NaF, Na_2CO_3, $ZnCl_2$ and sodium arsenate dibasic heptahydrate [$Na_2HAsO_4{\cdot}7H_2O$] were supplied by Sigma Aldrich (Taufkirchen, Germany). Sulfuric acid (H_2SO_4, 96%) was purchased from Honeywell (Seelze, Germany). Ascorbic acid (99%) and acetone (99.5%) were obtained from Panreac (Barcelona, Spain). Metal salts such as KH_2PO_4, $AlK(SO_4)_2$, KCl, $CdSO_4$, $CrCl_3$ and absolute ethanol were supplied by Merck KGaA (Darmstadt, Germany).

2.2. Synthesis of SiO_2@Mo(VI)-HS sorbent

The SiO_2@Mo(VI)-HS sorbent was synthesized using the classical sol–gel method as follows:

(i) First step: Preparation of alkaline CA solution. The alkaline cellulose solution (pH 10) was prepared by dissolving 0.2 g of cellulose acetate in a mixture of 25 mL acetone, 0.2 mL ammonium hydroxide, 0.3 g urea and 5 mL demineralized water.

(ii) Second step: Preparation of SiO_2/CTAB solution. One g of CTAB surfactant was dissolved in 40 mL ethanol under agitation for 10 min; 2.2 mL of TEOS were then added dropwise for 25 min under stirring at 25 °C.

(iii) Third step: Synthesis of CA-cross-linked SiO_2/CTAB nanospheres (SiO_2/CTAB-CA composite). The SiO_2/CTAB solution was added dropwise to the alkaline CA solution into a 250-mL neck-round flask under vigorous stirring for 15 h at 25 °C. The molar ratios TEOS:CTAB:CA were set at 1.0: 0.25: 0.1. The SiO_2/CTAB nano-spheres precipitated on cellulose fibers and the as-made solid sample of SiO_2/CTAB-CA was collected, filtered off and carefully washed with demineralized water and ethanol before being dried at 70 °C for 16 h in sealed condition before preparing the Mo(VI)-functionalized material.

(iv) Fourth step: Molybdate immobilization for SiO_2@Mo(VI)-HS synthesis. Ammonium molybdate salt (i.e., 0.25 g) was dissolved in a solution containing ethanol (35 mL), demineralized water (15 mL) and ammonium hydroxide (1.5 mL NH_3, 28–30% w/w); ammonium molybdate concentration was 4.0×10^{-3} M. A fixed amount of SiO_2/CTAB/CA composite (i.e., 1 g) was added to ammonium molybdate solution under vigorous stirring for 4 h at 25 °C. The SiO_2/CTAB/CA@Mo(VI) white filtrate was precipitated, filtered off and washed carefully with demineralized water and ethanol before being dried at 70 °C for 16 h in sealed condition. The organic compounds (sacrificed CA

template and CTAB) were carefully removed by calcination at 550 °C for 3 h (with a heating rate of 2 °C min^{-1}) to obtain SiO_2@Mo(VI)-HS sorbent. For sensor/sorbent application, the sorbent (SiO_2@Mo(VI)-HS, 1 g) was grinded in a mortar in the presence of ascorbic acid (powder, 10 mg). The mixture was referred as SiO_2@Mo(VI)-Asc.

2.3. Material characterization

The FTIR spectra for the synthesized SiO_2/CA-CTAB composite, SiO_2/CA/CTAB@Mo(VI) and the SiO_2@Mo(VI)-HS → As(V) were measured using Pye-Unicam Sp-883 PerkinElmer spectrophotometer, (Waltham, MA, USA). SEM images were collected using a high-resolution Environmental Scanning Electron Microscope (Quanta 250 FEG, FEI, Thermo Fisher Scientific, Hillsboro, OR, USA). TEM of the SiO_2@Mo(VI)-HS microporous was achieved using a JEOL JEM-1400 transmission electron microscope (JEOL, Ltd, Tokyo, Japan). The textural properties SiO_2@Mo(VI)-HS were measured using a BELSORP MIN-II analyzer through nitrogen adsorption at 77 K (MicrotracBEL Corp., Osaka, Japan). Particle size distribution and zeta potential of SiO_2@Mo(VI)-HS were determined by dynamic light scattering using a Nano Series Zeta Sizer (Malvern, Worcestershire, UK). The TGA/DTG analyses were acquired on a Shimadzu DT = TG-50 thermogravimeter, under N_2 atmosphere (Shimadzu, Kyoto, Japan). X-ray powder diffraction (XRD) measurements were carried out using a Philips X-ray generator model PW 3710–31 and a diffractometer with automatic sample changer model PW1775 (scintillation counter, Cu-target tube and Ni-filter at 40KV and 30 mA). UV spectra were collected using a UV–Vis-NIR spectrophotometer (Shimadzu 3700, Kyoto, Japan). Finally, the concentration of As(V) in solution was quantified via a calibration curve using UV spectrophotometer, double beam, CECIL CE7400, Aquarius at wavelength: 870 nm (Cecil Instrumentation Services Ltd., Cambridge, UK) and inductively coupled plasma – atomic emission spectrometer (iCAP 7000 SERIES, Thermo Fisher Scientific, Hillsboro, OR, USA).

2.4. Batch studies for As(V) ions sorption and detection

Sorption tests were carried out in batch mode. A fixed amount of sorbent (SiO_2@Mo(VI)-HS, m = 50 mg) was mixed with a volume of solution (V = 50 mL) containing As(V), at concentration C_0: 0.67 mmol As L^{-1} (sorbent dosage, SD: 1 g L^{-1}). The initial pH of the solution was varied between 1 and 10 with sulfuric acid or NaOH solutions. The flask was maintained under agitation for 60 min at 25 °C. The solution was separated from the sorbent by filtration on an Ahlstrom glass microfiber filter paper (1.2 mm pore size; 4.7 cm diameter). The residual As(V) concentration (C_{eq}, mmol As L^{-1}) in the filtrate was analyzed by spectrophotometry or ICP-AES and the sorption capacity (q_{eq}, mmol As g^{-1}) was deduced from the mass balance equation [56]:

$$q_e = (C_i - C_e)V/m \quad (1)$$

Other experiments such as uptake kinetics, sorption isotherms and the study of the effect of co-existing ions were conducted under the same procedures. Intermediary samples were collected for uptake kinetics, while initial As(V) concentration was varied up to 6.8 mmol As L^{-1} (at pH 1.8) for sorption isotherms. For the study of the effect of co-existing ions, arsenic solution (1 mg As L^{-1}) was completed by the addition of inorganic ions (at the concentration of 5 mg L^{-1}), other experimental conditions being identical.

Eluability and regeneration of the optical microcaptor were conducted through the contact of 100 mg of the SiO_2@Mo(VI)-HS composite with 100 mL of 50 mg As L^{-1} (i.e., 0.67 mmol As L^{-1}) solution under optimal experimental conditions. The solution was filtrated and the As loaded SiO_2@Mo(VI)-HS was washed with demineralized water; and As(V) was eluted with 1×10^{-3} M sodium bicarbonate (20 mL). The recovery efficiency (R_E %) was obtained from Eq. (2);

$$R_E(\%) = q_2/q_1 \times 100 \quad (2)$$

where (R_E) is the recovery efficiency (%), while q_1 and q_2 are the sorption capacities at the 1st and 2nd run, respectively. Sorption and desorption efficiencies were compared for eight successive cycles. The efficiency of the sorbent for As(V) removal from complex solutions was tested on two spiked solutions containing inorganic contaminants: a synthetic solution and a sample collected from a branch of the Nile river close to Menoufia governorate (Egypt). The solutions were spiked with As(V) at the concentration of 1 mg As L^{-1}.

2.5. Sensor testing

For sensor application, the sorbent (SiO_2@Mo(VI)-HS, 1 g) was grinded in a mortar in the presence of ascorbic acid (powder, 10 mg). The mixture was referred as SiO_2@Mo(VI)-Asc. The release of ascorbic acid contributes to reduce the complex formed between molybdate and arsenate, which, in turn, forms molybdenum oxide blue colored complex. The arsenomolybdate complex (associated with the formation of an α-Leggin anion) can be visually detected and/or quantified by spectrophotometry [57]. The sensor was added to As(V) solution at pH 1.8 (controlled with 0.2 M H_2SO_4 and NaOH solutions) with a material dosage of 1 g L^{-1} (typically: 210 mg for 20 mL). The mixture was mechanically shaken for 20 min at 25 °C with agitation speed close to 300 rpm. After reaching equilibrium in color development, the solid sensor was separated from the solution by filtration through a cellulose acetate filter paper. Arsenic content on the filter was qualitatively estimated by naked-eye observation, and quantified by UV–Vis spectrophotometry. In addition, As(V) residual concentration in the solution was measured using ICP-AES (and compared to the concentration of the initial solution); the standard deviation for As(V) concentration in solution was evaluated to 0.05%. A blank solution was also analyzed trice under the same experimental conditions to evaluate the blank standard deviation. The calibration of the different methods was performed by analysis of a series of As(V) standard solutions. This was used for determining the limit of detection (LOD) and the limit of detection (LOQ).

3. Results and discussion

3.1. Characterization of the synthesized materials

Various analytical methods have been used for characterizing the physical structure and the chemical composition of the SiO_2@Mo(VI)-HS sorbent (including intermediary compounds to illustrate the synthesis route). The preparation of the sorbent consists of the synthesis of silica microspheres by a sol–gel process, involving CTAB, and their precipitation at the surface of CA (sacrificed support): SiO_2/CA/CTAB composite. The binding of Mo(VI) (ammonium molybdate) allows synthesizing a Mo(VI)-impregnated support; the calcination of the material at 550 °C produces SiO_2@Mo(VI)-HS: the thermal degradation of organic compounds (the template) synthesizes hollow spheres bearing Mo(VI) oxides.

3.1.1. Morphology of sorbent and hollow spheres – SEM and TEM observations

The surface of microporous SiO_2@Mo(VI)-HS is characterized using SEM and HR-TEM analysis (Figs. 1 and 2): the material is characterized as a highly porous material (Fig. 1) constituted as the assembly of hollow spheres (Fig. 2). The porosity of the material is directly due to the calcination of the organic template (CA support sacrificed). The material can be defined as the agglomeration of nano-objects constituted of SiO_2 particles coated with Mo(VI) oxides; the size of interconnected nanoparticles is around 50–60 nm (though larger objects may be observed up to about 300–400 nm, through association).

Fig. 2 shows the TEM and HRTEM micrographs of microporous nanostructured SiO_2@Mo(VI)-HS composite. SiO_2 nano-spheres (of

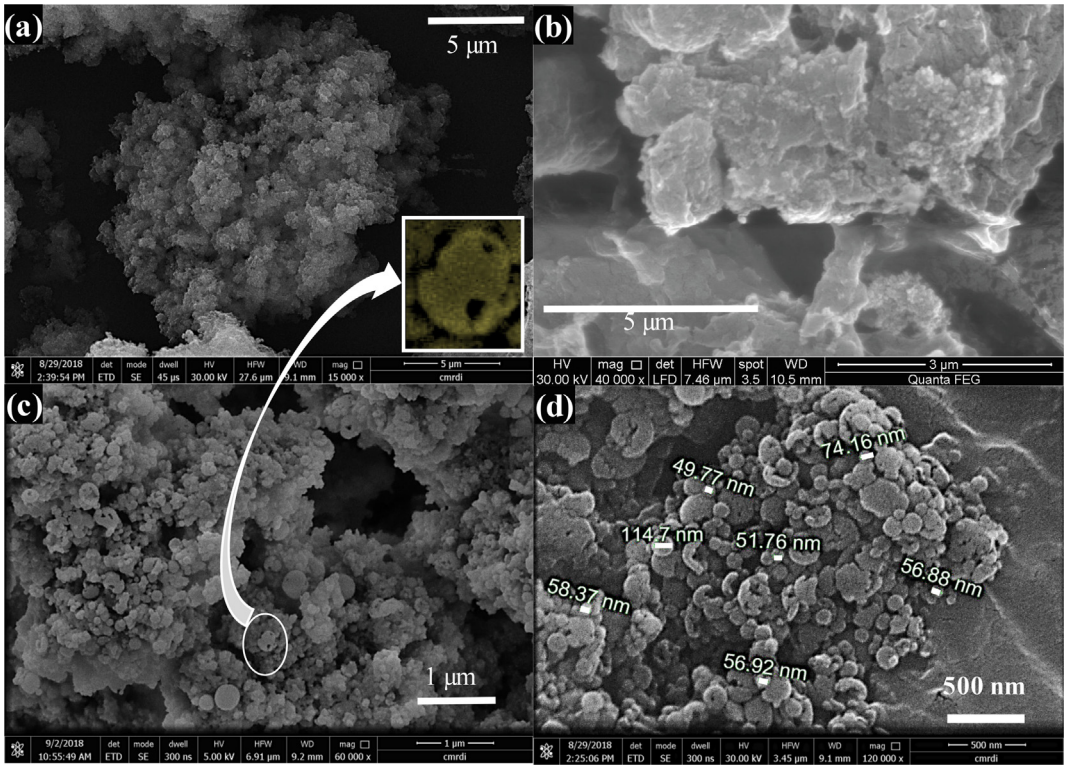

Fig. 1. SEM micrographs (at different magnifications) of SiO_2 @Mo(VI)-HS composite.

diameter close to 40–60 nm) are assembled to form a wagon wheel-like shape with numerous voids among the spheres. This may explain the high porosity (and specific surface area, see below) of this material. The connectivity between different SiO_2@MoO_3 nano-spheres might be due to the condensation between hydroxyl groups on adjacent spheres during the calcination. The HRTEM clearly displays the porous structure of the sorbent and confirms the existence of a hollow-spherical porous nanocomposite of molybdenum oxide-coated silica. Fig. 2(e & f) shows that SiO_2 nano-particles are completely covered with the MoO_3 layer; this confirms the synthesis of SiO_2@MoO_3 as also evidenced by XRD analysis (see below). Figure AM1 (see Additional Material Section) shows other TEM micrographs illustrating the reproducibility of hollow nanoparticles and their arrangement (formation of assemblies and channels).

TEM microphotographs show a hollow core appearing in Fig. 2e and f on the largest particles (30–108 nm), surrounded by a denser zone (thickness 40–60 nm), and covered by a lighter layer (19–30 nm). This "general" structure can be discussed through the following synthesis route. The first step in this process consists of the formation of the silica core (bearing mesopores) through the condensation of alkoxysilane under mild basic conditions. The preferential pore growth of inner silica core particles presumably occurred by the aggregation of subparticles (nuclei), followed by growth through cellulose acetate addition. In such pore formation, hydroxide ions induce a series of Si–O bond-breaking and bond-making processes that rearrange the high-energy bonds in the core, leading to the formation of cracks inside the particles. The second step of the synthesis results in the formation of concentric shells around the core. During bond re-arrangement, the micelle domains of the CTAB surfactant might simultaneously interact with the interior and exterior silica core of the sphere particles. Similar phenomena were described by Arnal et al. [58] and Zhang et al. [59]. The incorporation of Mo(VI) species to silica/CA-CTAB in the composition leads to the formation of double mesoporous core–shell silica/CA-CTAB/Mo(VI).

It is noteworthy that when the material is synthesized in the presence of an excess of molybdate on silica particles, the surface morphology and structure strongly change (Figure AM2) with formation of tablets of MoO_3 (77.64 mg Mo g^{-1} SiO_2). The complete covering of silica nanoparticles with MoO_3 tablets does not allow distinguish the surface of the support. Therefore, the amount of molybdate immobilized on the support is a critical parameter for defining the structure and texture of the composite.

It is noteworthy that these results are consistent with observations reported by Khoeini et al. [60] who prepared hollow mesoporous silica nanoparticles with a polystyrene-templating procedure associated with CTAB surfactant action. They obtained hollow nanoparticles with porous wall; the hollow chamber measured between 30 and 80 nm.

DLS measurements allowed identifying a bi-modal size distribution of SiO_2@Mo(VI)-HS particles: the predominant fraction (about 96%) is close to 69.5 nm, while some agglomerates have a larger size (4% in number) with a size close to 350 nm (Figure AM3). This is roughly consistent with the TEM observation reported on Fig. 2. The zeta potential analysis also shows a heterogeneous distribution of charges among the particles with a preponderant part of anionic nanoparticles: the global zeta potential is slightly negative (i.e., close to −10 mV). This is an important criterion to take into account for the interpretation of both the synthesis route and the final distribution and shape of particles. This global anionic charge can explain the limited agglomeration of nanoparticles. This is also important for the proper structuration of the material during the synthesis. The proper charges of cellulose acetate and CTAB, in relation with silanol groups at the surface of silica nanoparticles may explain the successive layers appearing on TEM (with different porous characteristics).

3.1.2. *Textural characteristics of the sorbent – BET analysis*

The textural characteristics of the sorbent (SiO_2@Mo(VI)-HS composite) were obtained using the N_2 adsorption/desorption technique. The BET-surface area (S_A), BJH pore volume (V_p), and the average pore diameter (D_p) were determined (Fig. 3a). The S_A is close to 715.5 m^2 g^{-1} while the porous volume is close to 0.295 cm^3 g^{-1}. The N_2 adsorption/desorption isotherm shows the common IV type, with an

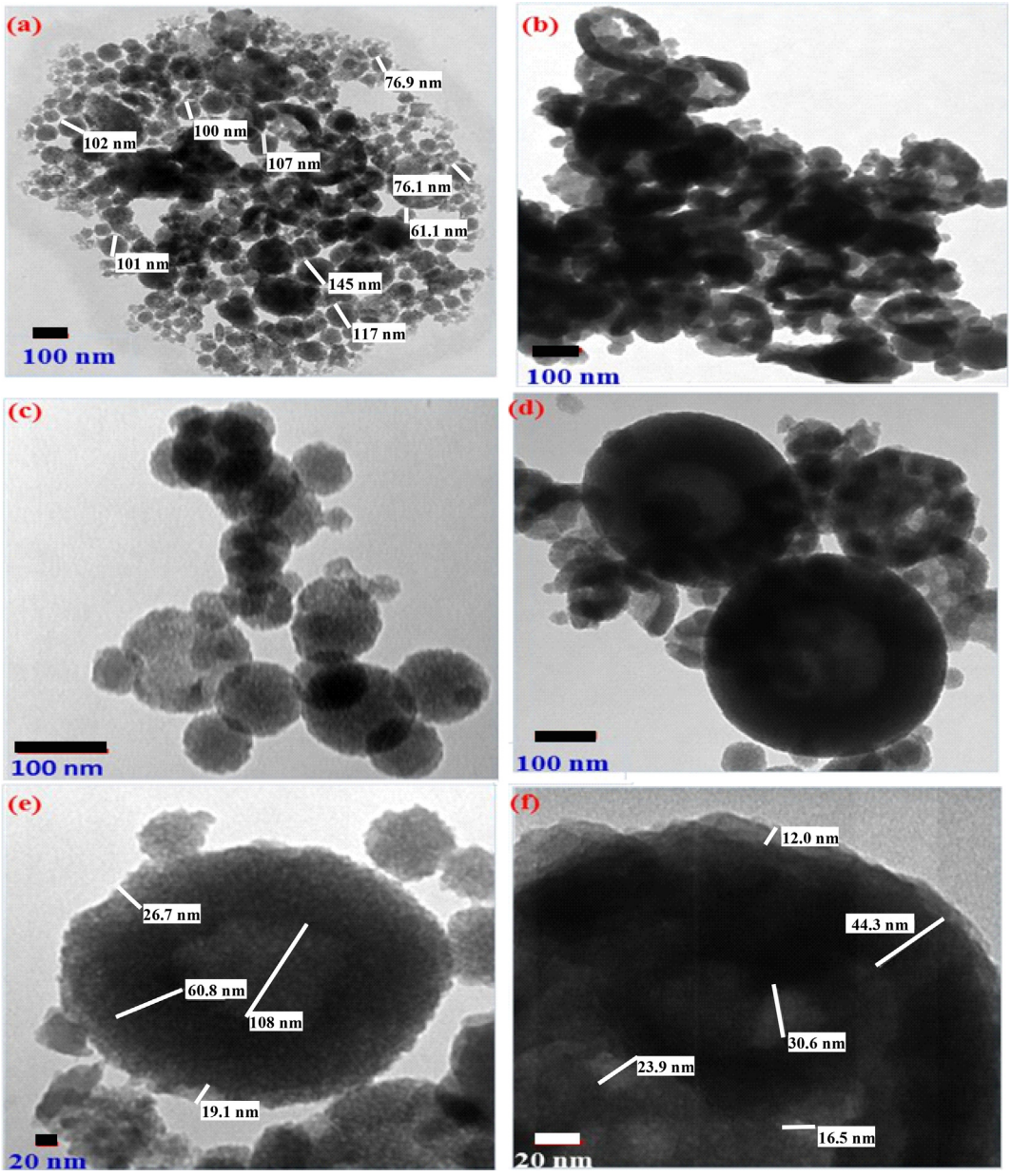

Fig. 2. TEM micrographs (at different magnifications) of SiO_2@Mo(VI)-HS composite.

extended hysteresis loop at low P/P_o (in the range 0.2 to 1.0). This result suggests the presence of micropores in SiO_2@Mo(VI)-HS. The steepness of the isotherm and the occurrence of capillary evaporation are associated with the formation of uniform pore diameter (1.41 nm) (major porous volume); however, another pore size close to 24 nm is due to inter-spheres holes (recorded on HRTEM observations). This analysis confirms the formation of interconnected hollow microspheres that gives the sorbent high porosity and specific surface area. This is particularly important for the fast response of the sensor for As(V) detection.

3.1.3. Thermogravimetric analysis

Fig. 3b shows the thermogravimetric analysis of SiO_2/CA/CTAB@Mo(VI) (including TGA and DTG). Different steps are identified in the thermogram. First, the weight loss while stabilizing the material at 38 °C was close to 6%. Between 38 °C and 120 °C the material loses 15.5% (total weight loss: 21.5%); this is directly associated with the desorption and release of water absorbed or immobilized in the porous network. Another weight loss (about 7.3%; total weight loss 28.8%) is observed between 202 °C and 310 °C: this corresponds to the thermal degradation of a fraction of the organic template (CTAB and CA may be concerned). The decomposition of free CTAB surfactant was reported at 232 °C, but when immobilized on zeolite degradation profile begun at lower temperature [61]. The next degradation step occurs between 310 °C and 383 °C: the material loses 4.8% (total weight loss: 33.6%). This loss is again associated to the degradation of a compound constitutive of the organic fraction of the composite, probably cellulose acetate [62]. It is noteworthy that the impregnation of paper with molybdate led to an increase in the temperature of degradation of the support [63]. The last phase in the degradation profile is observed between 383 °C and 900 °C with an additional weight loss close to 4.3% (total weight loss: 37.9%): this corresponds to the thermal degradation of the organic char. These different thermal transformations are correlated to three maximum peaks on the DTG curve: at 57 °C, 263 °C and 360 °C corresponding to dehydration, and degradation of CTAB and CA respectively. The incorporation of molybdate gives the composite higher onset temperature of decomposition.

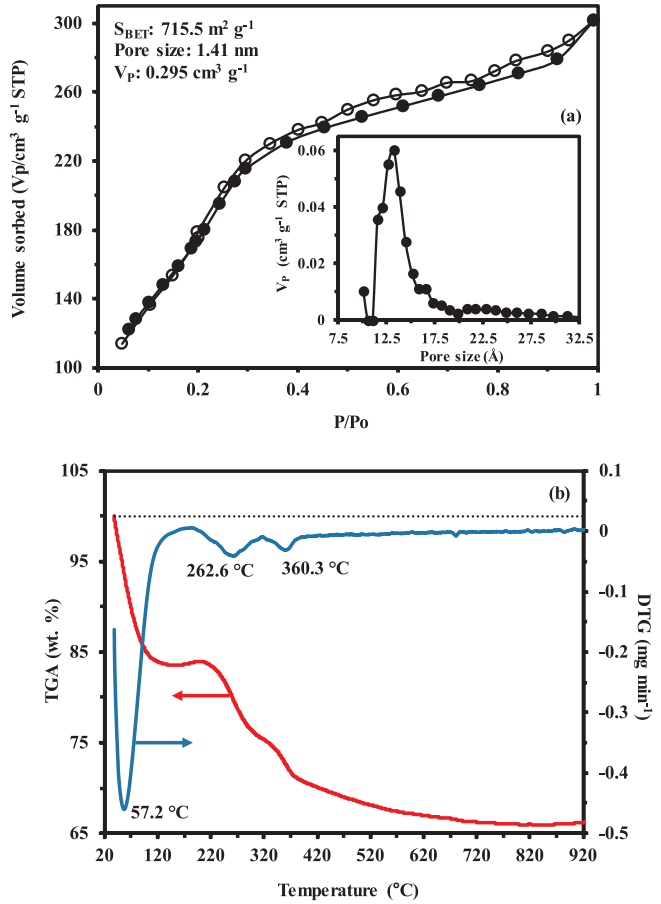

Fig. 3. Textural properties: (a) N_2 sorption/desorption isotherms (and pore size distribution, inset) and (b) TGA/DTG analysis (N_2 atmosphere, ramp: 10 °C min^{-1}) for SiO_2/CA/CTAB@Mo(VI)-HS composite before calcination at 550 °C for 3 h.

3.1.4. Surface characterization of the sorbent – FTIR spectroscopy

Fig. 4 shows the FTIR spectra of SiO_2/CA/CTAB composite, SiO_2@Mo(VI)-HS, and SiO_2@Mo(VI)-HS → As(V) (the sorbent after As(V) binding). The precursor (i.e., SiO_2/CA/CTAB composite, Fig. 4a) shows a broad band at 3434 cm^{-1}, which is assigned to the overlapping of hydrogen-bonded υ_{OH} stretching vibrations: hydroxyl groups are present at the surface of the material. In addition, a series of bands are observed at 2923.6 cm^{-1}, 2854 cm^{-1}, 1468 cm^{-1} and 1421 cm^{-1};

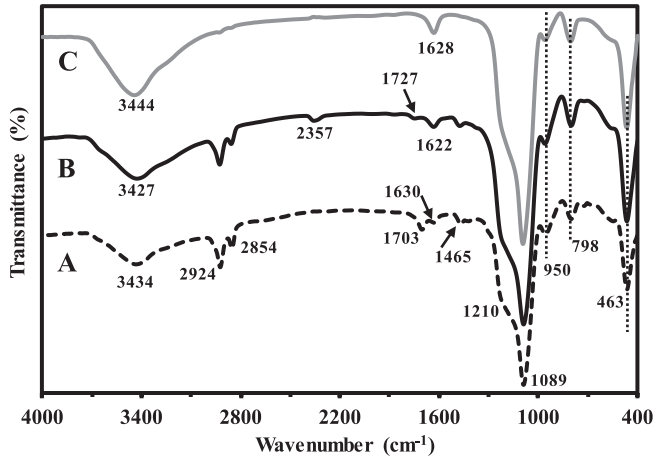

Fig. 4. FTIR spectra of SiO_2/CA/CTAB@Mo(VI) (*A*), SiO_2@Mo(VI)-HS (*B*) and SiO_2@Mo(VI)-HS-As(V) complex (*C*).

these bands are attributed to asymmetric υ_{C-H} stretching, symmetric υ_{CH3} frequencies and υ_{CH2} mode respectively [64]. On the other hand, the sharp peaks at 1630 cm^{-1} and 1703 cm^{-1} (tracers of cellulose acetate) are associated with stretching vibrations of C = O groups. The bands observed at 801 cm^{-1}, 723 cm^{-1} and 546.7 cm^{-1} are commonly assigned to Si-O-Si symmetric stretching vibrations [65]. The bands at 463 cm^{-1} and 957 cm^{-1} correspond to bending mode of Si-O bonds and symmetric stretching vibration of Si-OH respectively. Najafi et al. [66] assigned the band at 463 cm^{-1} to Si-O-Si rocking stretching. The strong intense broadband at 1088.6 cm^{-1} is assigned to Si-O-Si symmetric stretching vibration [66]. Carbonyl groups (free and bonded) have been identified at 1705 cm^{-1} and 1653 cm^{-1} for CA/silica composites [66], respectively (also identified at ≈ 1640 cm^{-1} and 1740 cm^{-1} [67] ; here, for SiO_2/CA/CTAB composite, the peaks appear at 1703 cm^{-1} and 1630 cm^{-1}, respectively. These peaks not present on raw silica are generally used for confirming the deposition of cellulose acetate on silica [66,67]; this is consistent with current results.

The FTIR spectrum of SiO_2/CA/CTAB@Mo(VI) (Fig. 4b) shows an additional new band at 2357 cm^{-1}; this band is usually associated with O═C═O or HO−C═O compounds. In addition, the υ_{OH} stretching vibration is shifted to 3427 cm^{-1} after the incorporation of MoO_3 groups within the material [35]. The peaks at 1703 cm^{-1} and 1630 cm^{-1} are shifted to 1727 cm^{-1} and 1622 cm^{-1}, respectively. These changes confirm the successful immobilization of molybdate groups on the composite surface. The immobilization of molybdate on silica was identified by the appearance of Mo-O stretching vibration at 774–905 cm^{-1}, corresponding to MoO_4^{2-} tetrahedrons [68]; the band does not appear on SiO_2/CA/CTAB@Mo(VI), probably because of superimposition with Si-O bands.

The FTIR analysis of SiO_2@Mo(VI)-HS → As(V) (Fig. 4c) shows the disappearance of a series of peaks, first at 2924 cm^{-1} and 2854 cm^{-1}, which correspond to C–H bonds. The disappearance of these peaks is directly correlated to the calcination of the SiO_2/CA/CTAB@Mo(VI) material (and the elimination of cellulose acetate/CTAB compounds). Similar trend were observed in the case of polystyrene-templated silica nano particles [60]: after calcination and polystyrene degradation) the C−H stretching vibrations disappear from FTIR spectra. The peaks at 1703 (or 1727) cm^{-1} and 1465 cm^{-1} also disappeared, probably due to calcination. The υ_{OH} stretching band is shifted to 3444 cm^{-1}. A band is observed at 1628 cm^{-1}, resulting from the shift of the band identified at 1630 and 1622 cm^{-1}; however, the increase in the intensity of this band suggests that the sorption of arsenate induces some changes at the surface of the sorbent. In the case of molybdate supported on PAM-PVA composite polymer hydrogel, Das and Sarkar [57] reported the appearance of a peak at 872.6 cm^{-1} after Mo(VI) binding, and its disappearance after As(V) sorption. These variations cannot be detected on Fig. 4; this is probably masked by the peaks associated to Si-O groups.

3.1.5. XRD analysis

Figure AM 4 shows the XRD patterns of SiO_2@Mo(VI)-HS composite together with SiO_2@Mo(VI)-HS → As. Fig. 5a confirms SiO_2@Mo(VI)-HS is poorly crystalline: a broad peak due to amorphous SiO_2 appears together with some grown narrow peaks corresponding to MoO_3. Molybdenum trioxide (MoO_3) is favorably obtained after releasing all organic matter by calcination at 550 °C, although molybdenum dioxide (MoO_2) may also appear. In addition, it was observed that Mo(VI) species are highly dispersed on silica. In contrast, after As(V) sorption (Fig. 5b), the visible narrow peaks completely disappear; this is due to the formation of blue molybdenum oxide (i.e., $Mo_2O_5{\cdot}H_2O$), which is coherent with conclusions raised in the literature [69].

3.2. As(V) ions sorption assays

3.2.1. Effect of pH

The pH of the solution is a critical criterion for visual detection and high sensitive removal of As(V) ions. The performance of the

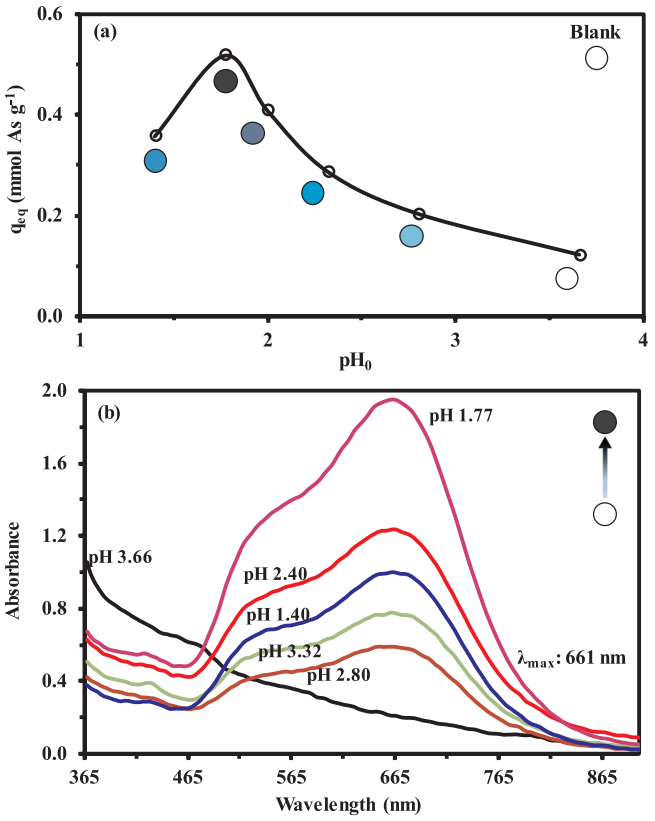

Fig. 5. Effect of initial pH on the sorption/spectrophotometric analysis of As(V) using SiO_2 @Mo(VI)-HS composite: (a) sorption capacity *vs.* initial pH; (b) UV spectra of the composite exposed to As(V) solutions at increasing pH (i.e., from 1.4 to 3.66) (C_0: 6.7 × 10^{-4} M; sorbent dosage, SD: 1 g L^{-1}; contact time: 60 min; Temperature, T: 25 °C).

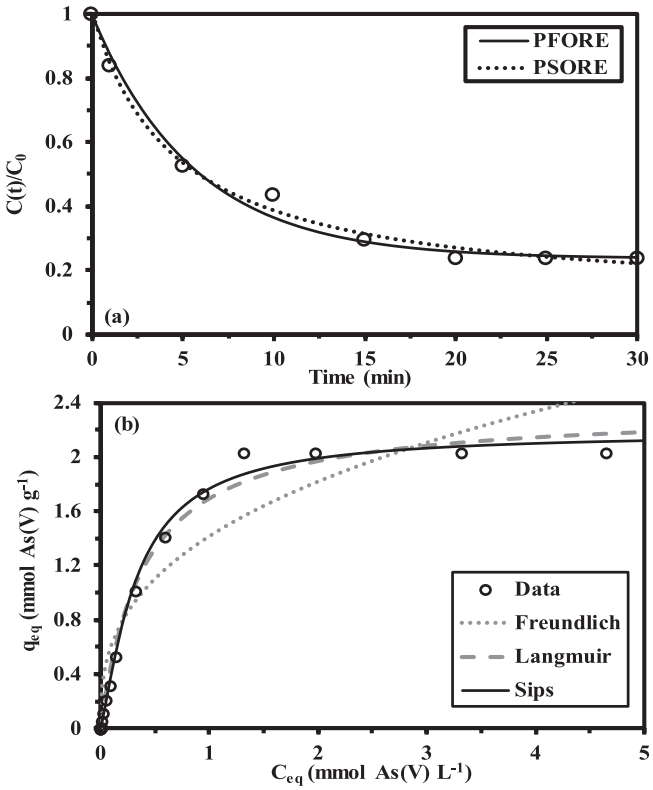

Fig. 6. As(V) uptake kinetics (with fitted lines using the PFORE and PSORE models) (a) and sorption isotherm (with fitted lines using the Freundlich, Langmuir and Sips equations) (b) using SiO_2@Mo(VI)-HS composite at pH 1.8 and T: 25 °C (SD: 1 g L^{-1}; C_0: 50 mg As L^{-1} for uptake kinetics; C_0: 0.02–500 mg As L^{-1} for sorption isotherms).

synthesized SiO_2@Mo(VI)-HS composite for As(V) sorption and its visual detection is qualitatively and quantitatively evaluated at different initial pH values (Fig. 5a). A distinctive change in color clearly appears at the surface of the sensor upon adding low concentrations of As(V) ions in the acidic pH region (between pH 1.4 and pH 3.7) under reductive conditions (i.e., in the presence of ascorbic acid; Fig. 5b). The highest capacity of the synthesized SiO_2@Mo(VI)-HS for As(V) binding is observed at pH 1.8. The speciation diagram (Figure AM5a) shows the predominance of neutral H_3AsO_4 species at pH 1. With pH increase, As (V) progressively deprotonates to form increasing fractions of anionic $H_2AsO_4^-$ species. The presence of ascorbic acid may also cause the reduction of arsenate to arsenite with formation of H_3AsO_3 (deprotonated species are significantly appearing above pH 7; not shown). Under selected experimental conditions, arsenic is essentially present as H_3AsO_3, H_3AsO_4 at low pH (below pH 2), while anionic As(V) species begins to predominate above pH 2.5 (Figure AM5a) [70–73]. The interaction of As(V) with molybdic acid solutions has been well documented. The concept was used for developing sensor and analytical systems using bismuth salt [74], or dyes [75] for improving the development of the color. In the presence of ascorbic acid, ammonium molybdenum forms the so-called molybdenum blue, which has a strong affinity for arsenate species [76]. The incorporation of adjuvants (such as sodium dithionite, potassium antimony tartrate) allowed the analytical speciation As(V)/As(III) [77]. Naked-eye detection of As(V) was also discussed in the case of amino-bearing resins functionalized by sorption of molybdate [78]; the contact of As(V) solutions with the resin in acidic solutions in the presence of a reducing agent (ascorbic acid) allowed turning the color of the resin to blue. The XPS analysis of the resin at the different stages of the reaction (Mo-loaded resin, As(V)/Mo-Resin and after reduction) clearly showed the formation of heteropoly acid (molybdenum blue) but also the formation of ternary complexes after As(V) binding. After reduction with ascorbic acid, several changes were detected including partial reduction of As(V) to As(III) and Mo(VI) to Mo(IV). Therefore, it is possible anticipating that the interpretation and modeling of As(V) binding on SiO_2@Mo(VI)-HS, in the presence of ascorbic acid, is made complex by these secondary chemical mechanisms. Under selected experimental conditions, the maximum sorption capacity is reached at pH 1.8; the sorption capacity attains 0.53 mmol As g^{-1}. These conditions correspond to the strongest density of blue color for naked-eye detection purpose. The mechanism involves the sorption of arsenate on molybdenum blue with possible mechanisms of reduction [76,78] and possible binding of anionic $HAsO_4^{2-}$ species [70,73,79].

3.2.2. *Effect of contact time*

Fig. 6a shows the relative decrease of As(V) concentration in function of time. Under selected experimental conditions, the equilibrium is reached with 20 min of contact: more than 90% is achieved within the first 15 min of agitation. This fast response can be explained by the micron-size of sorbent particles (60 nm), the high specific surface area (715 m^2 g^{-1}) and the pore size (1.4 nm larger than arsenate species; i.e., 248 pm). The calcination of the sorbent after Mo functionalization allows the pyrolysis of cellulose acetate and CTAB. This thermal degradation creates an additional porosity that increases the accessibility to Mo reactive groups. This contributes to fast uptake of As(V). This fast sorption is consistent with the short times required for color development in comparable systems [76,78]. This fast kinetics means that the mechanisms of resistance to film diffusion and to intraparticle diffusion are not playing a main role in the control of the binding of As(V) on the sorbent. Fig. 6a also shows the modeling of kinetic curves (solid and dotted lines) with the conventional pseudo-first order (PFORE, Eq. (3);

Table 1
Parameters of PFORE and PSORE models for As(V) uptake kinetics.

Parameter	PFORE	PSORE
$q_{eq,exp}$ (mmol As g^{-1})	0.51	0.51
$q_{eq,calc}$ (mmol As g^{-1})	0.509	0.602
k_i	0.178 min^{-1}	0.356 g $mmol^{-1}$ min^{-1}
R^2	0.989	0.993

[80]) and pseudo-second order (PSORE, Eq. (4); [81]) rate equations. The extension of these equations initially developed for modeling homogeneous reactions is successfully applied for fitting uptake kinetics in heterogeneous systems with the implicit hypothesis that rate coefficients are apparent constants that integrate the effective contributions of resistance to film and intraparticle diffusions.

$$\text{PFORE [80]: } q(t) = q_{eq,1}(1 - e^{k_1 t}) \tag{3}$$

$$\text{PSORE [81]: } q(t) = \frac{q_{eq,2}^2 \times k_2 \times t}{1 + q_{eq,2} \times k_2 \times t} \tag{4}$$

where $q_{eq(1\text{ or }2)}$ are the sorption capacity (q_{eq}, at equilibrium for PFORE and PSORE (respectively); $k_{(1\text{ or }2)}$ are the apparent rate coefficients for PFORE and PSORE (respectively). Table 1 reports the parameters for the models fitted to experimental curve; the parameters were determined by non-linear regression analysis (using Mathematica® software facilities). The determination coefficients (i.e., R^2) are very close for the two models (a little better for PSORE). However, the comparison of the calculated sorption capacities at equilibrium shows that the PFORE model is very close to the experimental value (compared with the PSORE that significantly overestimates the equilibrium sorption capacity). It is thus difficult discriminating between the two models: the PFORE is supposed to fit profiles controlled by physical sorption while the PSORE is usually associated with chemical sorption. Actually, the comparison of calculated sorption capacities at equilibrium for the two models with relevant experimental value shows that the pseudo-first order rate equation gives more appropriate fit.

3.2.3. Effect of As(V) ions concentrations

In order to evaluate the maximum sorption capacity of the sorbent, sorption isotherms were carried out at pH 1.8 (at the temperature of 25 °C). Fig. 6b shows the sorption isotherm: the uptake of As(V) ions by SiO_2@Mo(VI)-HS sharply increases before reaching a saturation plateau. It is noteworthy that the concentration of As(V) does not change the speciation of the metalloid: 73% of As(V) is present under the arsenic acid form (i.e., H_3AsO_4) while the mono-anionic species (i.e., $H_2AsO_4^-$) represents 27% (Figure AM5b). The maximum capacity is close to 2.03 mmol As g^{-1}. The sorption capacity (q_{eq}, mmol As g^{-1}) is plotted *vs.* the equilibrium concentration (q_{eq}, mmol As L^{-1}) for establishing sorption isotherm, which can be fitted using different models [82]. The Freundlich equation follows a power-like equation, which is not consistent with the saturation plateau observed in Fig. 6b. The Langmuir model (Eq. (6)) is described by a mechanistic equation that supposes the sorption sites to be energetically homogeneous and the sorbed molecules to be bound independently (not mutual interaction between species bound on vicinal reactive groups). The sorption is supposed to occur as a monolayer and the sorption capacity at saturation of this monolayer corresponds to maximum sorption capacity (q_m, mmol As g^{-1}). Introducing a third parameter in this mechanistic model allows, in certain cases, improving the quality of the fit; the Sips equation (Eq. (7)) corresponds to this empirical model.

$$\text{Freundlich [82]: } q = k_F C_{eq}^{1/n} \tag{5}$$

$$q_{eq} = \frac{q_{m,L} \times b_L \times C_{eq}}{1 + b_L \times C_{eq}} \tag{6}$$

Table 2
Parameters of Langmuir and Sips model for As(V) sorption isotherms.

Parameter	Freundlich	Langmuir	Sips
$q_{m,exp}$ (mmol As g^{-1})	2.03	2.03	2.03
k_F	1.416	–	–
$q_{m,calc}$ (mmol As g^{-1})	–	2.357	2.178
b (L $mmol^{-1}$)	–	2.567	4.231
n	2.767	–	0.773
R^2	0.926	0.992	0.996

$$\text{Sips [82]: } q = \frac{q_{m,S} \times b_S \times C_{eq_{eq}}^{1/n_S}}{1 + b_S \times C_{eq_{eq}}^{1/n_S}} \tag{7}$$

where $q_{m,L\text{ or }S}$ are the maximum sorption capacities (mmol As g^{-1}) for Langmuir and Sips equations (respectively), $b_{L\text{ or }S}$ is the affinity coefficients (L $mmol^{-1}$) for the Langmuir and the Sips equations (respectively), $n_{F\text{ or }S}$ is the energy coefficients for the Freundlich and the Sips equations (respectively), k_F is the Freundlich constant. These two models are represented by solid and dashed lines in Fig. 6b, with the parameters summarized in Table 2 (parameters obtained by non-linear regression analysis). Consistently with the very close values of determinations coefficients, the isotherm fits with the two models that are almost superimposed. The maximum sorption capacity determined with the Sips model is closer to the experimental value than the value obtained with the Langmuir equation. Table 3 summarizes the main properties of a series of sorbents for As(V) binding. This table shows that SiO_2@Mo(VI)-HS is one of the most efficient sorbents for As(V) removal from aqueous solutions.

3.2.4. Effect of temperature – thermodynamic parameters

The temperature may affect the distribution of solute between the liquid and solid phases. Figure AM6 shows the comparison of As(V) sorption isotherms at pH 1.8 for different temperatures, in the range 25–40 °C (including the repetition of T: 25 °C). In this limited range of temperatures, the variations are relatively weak but sufficient to demonstrate that the reaction is endothermic: the sorption capacity increases with temperature. The Langmuir coefficient b_L, determined at the different temperatures, is used in the Van 't Hoff equation (Eq. (8)) for calculating the thermodynamic parameters (i.e., ΔH°, enthalpy change, kJ mol^{-1}; ΔS°, entropy change, J mol^{-1} K^{-1}; and ΔG°, free Gibbs energy change, kJ mol^{-1}):

$$\ln b_L = \frac{\Delta H^\circ}{RT} + \frac{\Delta S^\circ}{R} \tag{8a}$$

$$\Delta G^\circ = -\Delta H^\circ + \Delta S^\circ \tag{8b}$$

The enthalpy change (ΔH°: 16.87 kJ mol^{-1}) is positive; this confirms the endothermic behavior of As(V) sorption on SiO_2@Mo(VI)-HS surface. The entropy change is also positive (ΔS°: 122 J mol^{-1} K^{-1}). This means that the randomness of the system (sorbent/solute) increases after sorption (in acidic solutions and in the presence of the reducing agent); probably due to the fast formation of hetero polyacids under these selected conditions. The free energy (Gibbs) change varies between −19.48 and −21.92 kJ mol^{-1}: the negative values indicate that the reaction is spontaneous and becomes more favorable with the increase of the temperature. The fact that $|\Delta H^\circ| < |-T\Delta S^\circ|$ confirms that the sorption of As(V) is controlled by entropic changes rather than by enthalpic changes. Increasing the temperature enhances As(V) sorption and simultaneously speeds up the development of the color: color intensity is detected by naked-eye within 10 min at T: 40 °C.

3.2.5. Sensor application and limit of detection

The preciseness of As(V) detection using SiO_2@Mo(VI)-HS sensor was performed using a simple sensitive sequential quantification of the color for sorbent/solution suspensions with increasing concentrations

Table 3
Comparison of As(V) sorption capacities onto various sorbents .

Sorbent	pH	Contact time (min)	As(V) sorption capacity (q_m or q_L, mmol As g^{-1}).	Ref.
Fe(III)-Ti(IV) oxide	7.0	360	0.19	[87]
Fe-Mn binary oxide	4.8	1440	0.96	[88]
Fe-Cu binary oxide	7.0	1440	1.10	[89]
CuO nanoparticles	6.0–10.0	600	0.30	[90]
$Al_2O_3/Fe(OH)_3$	6.62–6.74	2880	0.49	[91]
Fe-Zr binary oxide	7.0	2940	0.62	[92]
Molybdenum(VI)-chitosan-TEPA	2.5–3.5	6	1.35	[93]
Iron-zeolites-activated carbon	7.0–11.0	2880	1.05	[94]
Eggshell/goethite/α-MnO_2	5.0	60	0.63	[95]
Fe(III)/La(III)-chitosan	3.0–8.0	45	1.46	[96]
Al-HDTMA-sericite	5.5	1440	0.01	[97]
Cell-N-Cu	8.4	5	1.32	[38]
SiO_2@Mo(VI)-HS	1.8	20	2.03	Present work

of As(V) concentrations (from 2.6 × 10^{-7} to 3.3 × 10^{-3} M). The UV–Vis reflectance spectra were collected to detect the changes associated with the interaction of SiO_2@Mo(VI)-HS with As(V) and to the formation of the complex [SiO_2@Mo(VI)-HS → As(V)]. The color signal fast revealed by ascorbic acid allows correlating the color intensity to the effective arsenic concentration in the solution. Molybdate layer coated silica surfaces develops a blue color through the formation of a hetero-poly-acid between Mo(VI) and As(V) ions in presence of ascorbic acid. Once the SiO_2@Mo(VI)-HS composite is in contact with As(V) ions solution, Mo(VI) is reduced to lower valence state Mo(IV) along with the reduction of As(V) to As(III) [78].

The change in the color (measured by absorbance spectral responses of the [SiO_2@Mo(VI)-HS → As(V)] complex) is recorded at λ_{max} = 661 nm (Fig. 7a). The relation between As(V) concentrations and absorbance is represented in Fig. 7b. The calibration might be limited to absorbance lower than 1; this corresponds to the range of concentration where the signal is linear against As(V) concentration (i.e., 2.6 × 10^{-7} to 6.6 × 10^{-6} M) at pH 1.8 (insert in Fig. 7b). The limit of detection (LOD) of As(V) ions using SiO_2@Mo(VI)-HS sensor was assessed from the linear part of Fig. 7b, according to Eq. (9) [79]:

$$LOD = 3 \times \frac{StD}{slope} \quad (9a)$$

$$LOQ = 10 \times \frac{StD}{slope} \quad (9b)$$

where *StD* is the standard deviation on blank analysis StD (triplicate analysis) on blank analysis (3 measures) and *slope* is the slope of the linear section of the curve. Here the standard deviation is StD = 0.005686 while the slope is 0.0517 or 0.0571 (depending on the range of concentration and the inclusion of the initial point). This means that the LOD is close to 0.3–0.33 μM (i.e., close to 25 μg L^{-1}), while the LOQ is around 1.00–1.10 μM (i.e., close to 75 μg L^{-1}). This is consistent with the level of detection reported on molybdate-loaded synthetic resin for As(V) in the presence of ascorbic acid [78].

These results show that the microporous SiO_2@Mo(VI)-HS composite can detect trace amounts of As(V) in water. However, the limit concentration for As in drinkable water is 10 μg As L^{-1}. This means that the sensor is not sufficient for achieving drinkable water levels and livestock drinking water [83]. US EPA and FAO recommend a 0.1 mg L^{-1} limit concentration for As in irrigation water [84].

3.2.6. Selectivity assays

To assert the applicability of the proposed SiO_2@Mo(VI)-HS optical microporous sensor it is necessary evaluating its ability to selectively detect and remove As(V) ions from multi-component aqueous solutions. Fig. 8a shows the results for the sorption and sensing of As(V) at the concentration of 10 μM in the presence of an excess of interfering ions (at constant concentration: 5 mg L^{-1}). The list of selected interfering

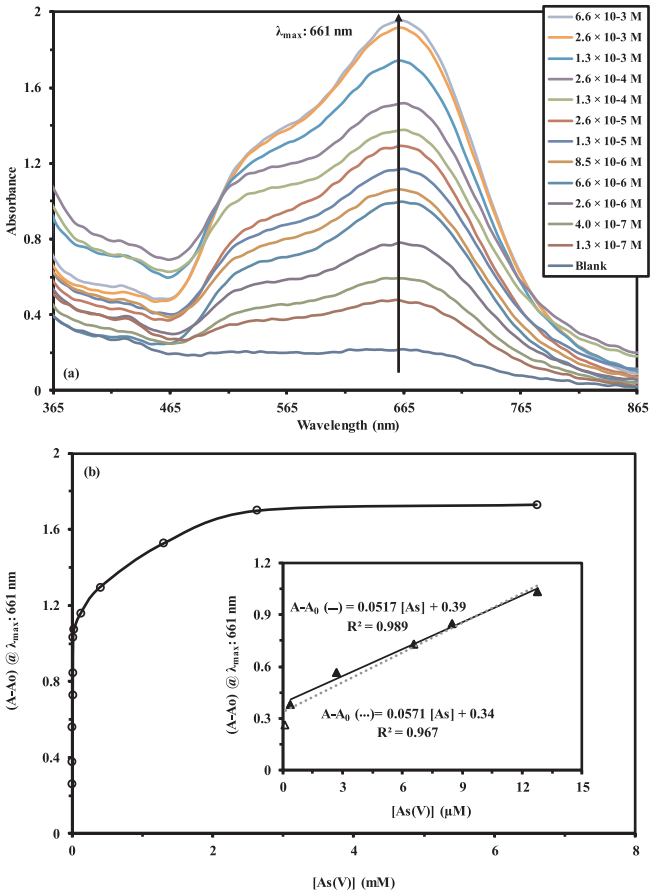

Fig. 7. Effect of As(V) concentration on: (a) the UV spectra response of the SiO_2@Mo(VI)-HS composite, and (b) the corrected absorbance (@ λ_{max}: 661 nm; pH 1.8; T: 25 °C; Time: 30 min; C_0(As): 1.25 × 10^{-7} – 6.60 × 10^{-3} M, inset: focus on the initial linear section).

ions counts: phosphate, sulfate, silicate, nitrate, bromide, chloride, sodium, fluoride, potassium, calcium, magnesium, iron, copper, cobalt, nickel, manganese, aluminum and lead. The analytical test was performed at the optimum pH (i.e., pH 1.8). The results clearly demonstrate that in most cases As(V) is not affected by the presence of an excess of interfering ions: the removal efficiency exceeds 95% and the sorption of these ions remains negligible. A few interfering ions are identified: Fe(II) > silicate > sulfate > phosphate. The interfering effect is probably expressed by different mechanisms. Indeed, for silicate, sulfate and phosphate ions their hydrated ionic size if very close (or higher) to the ionic size of hydrated arsenate (Table AM1, see AMS); the level of interference is correlated to the proximity in the ionic size

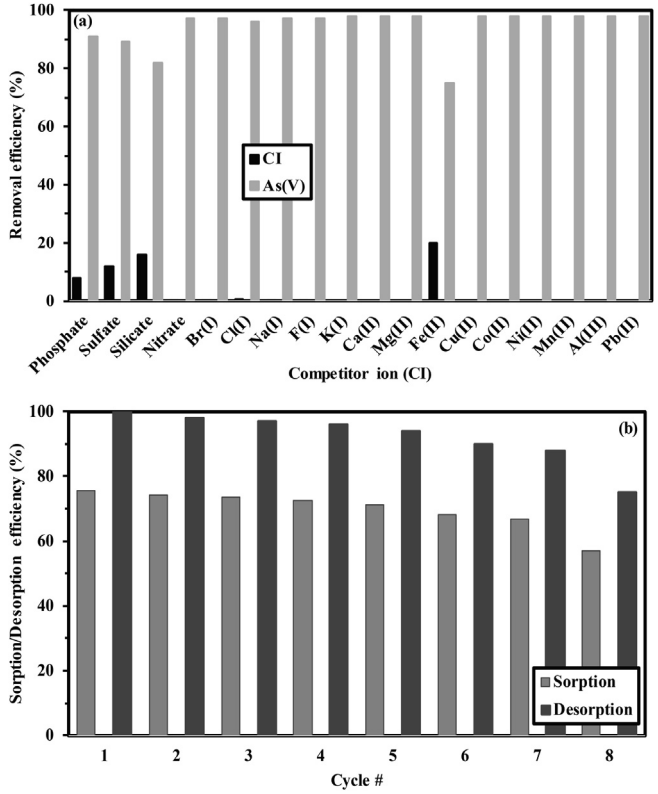

Fig. 8. (a) Effect of coexisting-ions (CI) on the selectivity of As(V) sorption/detection using SiO_2 @Mo(VI)-HS composite (C_0: 1 mg As L^{-1}; C_0(CI): 5 mg L^{-1}; pH: 1.8; SD: 1 g L^{-1}; Temperature: 25 °C; Time: 30 min), and (b) Effect of the recycling of SiO_2 @Mo(VI)-HS composite on the recovery of As(V) over 8 cycles of sorption/desorption.

of hydrated species. On the other hand, in the case of Fe(II) the hydrated ion has a much lower ionic radius. Another contribution to this competition effect consists of the specific interaction that may exist between the anion with molybdate (especially silicate and phosphate). The competitor effect of phosphate and silicate (to a lesser extent) was reported by Dambies et al. [39,40] for the binding of As(V) onto molybdate-impregnated chitosan beads.

For these four interfering ions, the removal efficiency remains below 20% and the loss in As(V) never exceeds 25%. Silicate and Fe(II) at concentrations up to 0.1 mM and 5 mM, respectively, interfere with As(V) sorption. The selectivity of the microporous-sorbent can be ascribed to its high binding affinity for the target co-existing ions and the stability of the formed SiO_2@Mo(VI)-HS → As(V) complex. This result confirms the fast binding interactions and the stability of the target ion-to-sorbent complex on the pore surfaces under optimal pH conditions, leading to the selective removal of As(V) ions in contaminated samples. The stability constant (log K_{As}) of the formed SiO_2@Mo(VI)-HS → As(V) complex at a specific pH value has a significant effect on As ion-selectivity of the microporous SiO_2@Mo(VI)-HS sorbent, particularly in high dilute concentration of As(V), compared with competitive matrices. The value of log K_{As} can be calculated using Eq. (10) [85];

$$logK_{As} = [SiO_2@Mo \rightarrow As]_s / [SiO_2@Mo]_s \times [As]_L \quad (10)$$

where $[As]_L$ and $[L]_S$ represent the concentration of [As] in 50 mL solution (3.4 mmol L^{-1}), and the total Mo(VI) content in SiO_2@Mo(VI)-HS (0.17 mM), respectively. $[ML]_L$ is the concentration of As loaded on SiO_2@Mo(VI)-HS sorbent. The determination of the stability constants was carried out at 25 °C and pH 1.8. Results from the binding constants (log K_{As}) of the complex formed upon addition of As(V) ions was 3.4 at the optimal pH value. This value means that As(V) ions strongly bind onto the microporous SiO_2@Mo(VI)-HS surface preferentially to

Table 4
Removal of As(V) ions in simulated synthetic and real surface water sample at pH 1.8, SiO_2@Mo(VI)-HS weight of 50 mg, solution volume of 50 mL, 30 min equilibrium time at 25 °C.

Sample	Synthetic solution			Real sample		
Interfering ion	C_0 (mg L^{-1})	C_{eq} (mg L^{-1})	SC	C_0 (mg L^{-1})	C_{eq} (mg L^{-1})	SC
As(V)	1	0.04	1	1	0.07	1
PO_4^{3-}	5.26	4.48	138	0.14	0.12	79.7
SO_4^{2-}	29.9	26.5	187	20.76	19.13	156
Cl^-	9.8	9.4	564	36.84	34.8	227
NO_3^-	5.8	5.7	1368	0.36	0.35	465
CO_3^{2-}	5.0	4.6	276	24.8	23.4	222
F^-	5.2	5.2	∞	0.52	0.51	678
Na(I)	44.7	44.2	2122	28.4	28.3	3760
K(I)	5.02	4.97	2386	5.62	5.6	3720
Ca(II)	20.6	19.6	470	32.4	32.28	3574
Mg(II)	22.0	21.9	5256	17.8	17.7	2352
Fe(III)	2.00	1.95	936	0.11	0.09	59.8
Mn(II)	2.09	2.09	∞	0.09	0.09	∞
Al(III)	5.00	4.98	5976	0.07	0.07	∞
Zn(II)	5.7	5.7	∞	0.09	0.09	∞
Pb(II)	5.0	5.0	∞	–	–	–
Cd(II)	5.02	5.01	12,024	–	–	–
Hg(II)	4.98	4.97	11,928	–	–	–
Ni(II)	5.0	5.0	∞	–	–	–
Co(II)	5.3	5.2	1248	–	–	–
Cr(III)	4.5	4.5	∞	–	–	–
pH	1.8			1.8		

∞: corresponding to interfering ions that are not sorbed on SiO_2@Mo(VI)-HS.

competitive ions.

In addition, the application of SiO_2@Mo(VI)-HS as an optical microporous sensor was examined in both simulated synthetic and real samples under optimal experimental conditions. The simulated synthetic sample with a standard solution of 1.0 mg L^{-1} As(V) ions (Table 4). The results indicate that SiO_2@Mo(VI)-HS composite could be used as a good sensor/sorbent for removal/sensing of As(V) ions from polluted environments. To complete the assessment of the applicability of the synthesized SiO_2@Mo(VI)-HS composite, a sample of the real surface water obtained from River Nile, at Menoufia, Egypt, was injected with a known quantity of arsenic (i.e., 1.0 mg L^{-1} As(V)). The analyses were carried out using ICP-AES, as reported in Table 4. Arsenic was efficiently sorbed: the sorption efficiency reaches 96% and 93% for synthetic solution and for Nile river sample, respectively. The presence of an excess of other cations (metal cations) and anions has a limited impact on As(V) removal. The selectivity coefficient (SC) is defined by the ratio of the distribution ratios for As(V) over element:

$$SC = \frac{D_{As}}{D_{element}} = \frac{q_{eq,As} \times C_{eq,element}}{C_{eq,As} \times q_{eq,element}} \quad (11)$$

The comparison of SC values are difficult because the level of concentrations of the different co-ions are different; however, some trends can be identified. Other metal ions are not bound: the change in concentration does not exceed a few percent (less than 5% in the case of synthetic solution and even less for Nile river sample). The anions are more efficiently bound; however, sorption efficiency does not exceed 12% (for SO_4^{2-} from synthetic solution). The highest SC values are obtained for Cd(II) and Hg(II) (around 12000), Mg(II) and Al(V) (in the range 5000–6000) and for monovalent cations (such as Na(I) and K(I), around 2200), for synthetic solution.

On the opposite hand, the lowest SC values are reported for phosphate (i.e., 138) and sulfate (i.e., 187) anions. This is consistent with previous conclusions on the effect of anions having hydrated ionic radius close (sulfate anions: 230 pm) or higher (phosphate anions: 323 nm) than As(V) (248 pm), and specific molybdate-phosphate (or silicate) interactions. Figure AM7 shows an illustration of sorption test

carried out on Nile river sample.

3.2.7. Reusability assays

The competitiveness and effectiveness of the support for both sorption and sensor application requires the material to be easily re-generated and to be re-usable. Fig. 8b compares the sorption and desorption efficiencies for the recovery of As(V) for eight successive cycles, using 1 mM $NaHCO_3$ solution as the stripping agent [74]. The system shows remarkable stability for the first 5 cycles: the sorption efficiency slightly decreases (from 75.5 to 71.3%, for the first run) while the desorption efficiency decreases from 100% to 94%. Induced by fractional dissolution of both SiO_2 and MoO_3 after regeneration in alkaline media, the removal performance of arsenic was decreased due to the exfoliation and dissolution of MoO_3 film from silica particles surface [86]. After the fifth cycle, the loss in efficiencies slightly increases, especially in the eighth cycle: sorption efficiency decreases to 57.1% and the desorption efficiency tends to 75%.

4. Conclusion

This study describes the development of nano-structured porous Mo (VI)-coated silica (SiO_2@Mo(VI)-HS) characterized by its specific morphology (i.e., hollow-spheres) and high surface area (i.e., 715.5 m^2 g^{-1}) for sensing and removing As(V) ions from real samples. The synthesized composite was well characterized by various techniques (XRD, FTIR, SEM, TEM, N_2 adsorption/desorption, and thermal analysis).

The pH is a critical parameter for the activity of the support for both As(V) sorption and detection: optimum value is found close to 1.8. Uptake kinetics is fitted by the pseudo-first order rate equation; the equilibrium is reached within 20–25 min of contact. Sorption isotherms are modeled by the Langmuir equation: maximum sorption capacity reaches up to 2 mmol As g^{-1} at 25 °C. The sorption is endothermic (positive value of enthalpy change), spontaneous (negative value of free energy change), and controlled by entropic changes. The ions that affect the most significantly As(V) binding are Fe (II) > silicate > sulfate > phosphate. Arsenic can be readily desorbed from sorbent using 1 mM $NaHCO_3$ solution, SiO_2@Mo(VI)-HS can be re-used for a minimum of 5 cycles with negligible loss in sorption and desorption performances; the system maintains good properties for at least 8 cycles.

In addition, to As(V) sorption properties, the material can be used (in the presence of ascorbic acid) for naked-eye detection of arsenate traces. The spectral response for [SiO_2@Mo(VI)-HS → As(V)] complex shows a maximum absorbance at λ_{max} = 661 nm. The LOD is close to 0.33 μM while the LOQ approaches 1 μM (i.e., approximately 25 and 75 μg L^{-1}, respectively).

Acknowledgments

EG acknowledges Institut Français d'Egypte (IFE, French Government, and Ministère des Affaires Etrangères and Ministère de l'Enseignement et de la Recherche) for supporting the collaboration between IMT – Mines Ales and Nuclear Materials Authority.

Appendix A. Supplementary data

Supplementary data to this article can be found online at https://doi.org/10.1016/j.cej.2020.124439.

References

[1] ATSDR, Arsenic Toxicity: Case Studies in Environmental Medicine, Agency for Toxic Substances and Disease Registry, in: US Department of Health and Human Services, Washington, DC, USA, 2002, pp. 39.
[2] T.M. Clancy, K.F. Hayes, L. Raskin, Arsenic waste management: A critical review of testing and disposal of arsenic-bearing solid wastes generated during arsenic removal from drinking water, Environ. Sci. Technol. 47 (2013) 10799–10812.
[3] R. Eisler, Arsenic Hazards to Fish, Wildlife, and Invertebrates: A Synoptic Review, in: Contaminant Hazard Reviews, Laurel, MD, 1988.
[4] S.J.S. Flora, Handbook of Arsenic Toxicology, Academic Press, Elsevier, Oxford (U. K.), 2015, 752 pp.
[5] D. Panagiotaras, D. Nikolopoulos, Arsenic occurrence and fate in the environment; A geochemical perspective, J. Earth Sci. Clim. Change, 6 (2015) 9 Pages – Art. N° 269.
[6] M. Bissen, F.H. Frimmel, Arsenic – a review – Part 1: Occurrence, toxicity, speciation, mobility, Acta Hydroch. Hydrob. 31 (2003) 9–18.
[7] J.C. Ng, J.P. Wang, A. Shraim, A global health problem caused by arsenic from natural sources, Chemosphere 52 (2003) 1353–1359.
[8] J.C. Saha, A.K. Dikshit, M. Bandyopadhyay, K.C. Saha, A review of arsenic poisoning and its effects on human health, Crit. Rev. Environ. Sci. Technol. 29 (1999) 281–313.
[9] P.L. Smedley, D.G. Kinniburgh, Source and behaviour of arsenic in natural waters, 2001.
[10] H.M. Anawar, J. Akai, K. Komaki, H. Terao, T. Yoshioka, T. Ishizuka, S. Safiullah, K. Kato, Geochemical occurrence of arsenic in groundwater of Bangladesh: sources and mobilization processes, J. Geochem. Explor. 77 (2003) 109–131.
[11] T. Balaji, T. Yokoyama, H. Matsunaga, Adsorption and removal of As(V) and As(III) using Zr-loaded lysine diacetic acid chelating resin, Chemosphere 59 (2005) 1169–1174.
[12] S. Chakravarty, V. Dureja, G. Bhattacharyya, S. Maity, S. Bhattacharjee, Removal of arsenic from groundwater using low cost ferruginous manganese ore, Water Res. 36 (2002) 625–632.
[13] K.P. Singh, A. Malik, D. Mohan, S. Sinha, Multivariate statistical techniques for the evaluation of spatial and temporal variations in water quality of Gomti River (India) – a case study, Water Res. 38 (2004) 3980–3992.
[14] S. Kundu, A.K. Gupta, Sorption kinetics of As(V) with iron-oxide-coated cement – a new adsorbent and its application in the removal of arsenic from real-life groundwater samples, J. Environ. Sci. Health., Part A Environ. Sci. Eng. Toxic Hazard. Subst Control 40 (2005) 2227–2246.
[15] A.E. Pagana, S.D. Sklari, E.S. Kikkinides, V.T. Zaspalis, Microporous ceramic membrane technology for the removal of arsenic and chromium ions from contaminated water, Microporous Mesoporous Mater. 110 (2008) 150–156.
[16] K. Phan, S. Sthiannopkao, K.-W. Kim, M.H. Wong, V. Sao, J.H. Hashim, M.S.M. Yasin, S.M. Aljunid, Health risk assessment of inorganic arsenic intake of Cambodia residents through groundwater drinking pathway, Water Res. 44 (2010) 5777–5788.
[17] WHO, Guidelines for drinking-water quality, 4th ed., World Health Organization, Geneva (Switzerland), 2011, 541 pp.
[18] H.M. Baioumy, Preliminary data on cadmium and arsenic geochemistry for some phosphorites in Egypt, J. Afr. Earth Sci. 41 (2005) 266–274.
[19] S.M. Shaheen, E.E. Kwon, J.K. Biswas, F.M.G. Tack, Y.S. Ok, J. Rinklebe, Arsenic, chromium, molybdenum, and selenium: geochemical fractions and potential mobilization in riverine soil profiles originating from Germany and Egypt, Chemosphere 180 (2017) 553–563.
[20] R. Devi, E. Alemayehu, V. Singh, A. Kumar, E. Mengistie, Removal of fluoride, arsenic and coliform bacteria by modified homemade filter media from drinking water, Bioresour. Technol. 99 (2008) 2269–2274.
[21] T. Halttunen, M. Finell, S. Salminen, Arsenic removal by native and chemically modified lactic acid bacteria, Int. J. Food Microbiol. 120 (2007) 173–178.
[22] P. Mondal, C.B. Majumder, B. Mohanty, Treatment of arsenic contaminated water in a laboratory scale up-flow bio-column reactor, J. Hazard. Mater. 153 (2008) 136–145.
[23] A. Oehmen, R. Valerio, J. Llanos, J. Fradinho, S. Serra, M.A.M. Reis, J.G. Crespo, S. Velizarov, Arsenic removal from drinking water through a hybrid ion exchange membrane – coagulation process, Sep. Purif. Technol. 83 (2011) 137–143.
[24] Y. Song, G.M. Swain, Development of a method for total inorganic arsenic analysis using anodic stripping voltammetry and a Au-coated, diamond thin-film electrode, Anal. Chem. 79 (2007) 2412–2420.
[25] S. Kagaya, E. Maeba, Y. Inoue, W. Kamichatani, T. Kajiwara, H. Yanai, M. Saito, K. Tohda, A solid phase extraction using a chelate resin immobilizing carboxymethylated pentaethylenehexamine for separation and preconcentration of trace elements in water samples, Talanta 79 (2009) 146–152.
[26] A. Negrea, A. Popa, M. Ciopec, L. Lupa, P. Negrea, C.M. Davidescu, M. Motoc, V. Minzatu, Phosphonium grafted styrene-divinylbenzene resins impregnated with iron(III) and crown ethers for arsenic removal, Pure Appl. Chem. 86 (2014) 1729–1740.
[27] A. Negrea, M. Ciopec, P. Negrea, L. Lupa, A. Popa, C.M. Davidescu, G. Ilia, Separation of As-V from aqueous solutions using chelating polymers containing Fe-III-loaded phosphorus groups, Open Chemistry 13 (2015) 105–112.
[28] T. Kajiwara, E. Maeba, S. Kagaya, Y. Inoue, W. Kamichatani, H. Yanai, M. Saito, K. Tohda, Solid phase extraction of arsenic using an iron (III)-supported chelate resin immobilizing carboxymethylated pentaethylenehexamine, Bunseki Kagaku 60 (2011) 629–634.
[29] M.J. Haron, W. Yunus, N.L. Yong, S. Tokunaga, Sorption of arsenate and arsenite anions by iron(III)-poly(hydroxamic acid) complex, Chemosphere 39 (1999) 2459–2466.
[30] H. Matsunaga, T. Yokoyama, R.J. Eldridge, B.A. Bolto, Adsorption characteristics of arsenic(III) and arsenic(V) on iron(III)-loaded chelating resin having lysine-N-α, N-α-diacetic acid moiety, React. Funct. Polym. 29 (1996) 167–174.
[31] A. Shahat, H.M.A. Hassan, H.M.E. Azzazy, M. Hosni, M.R. Awual, Novel nano-conjugate materials for effective arsenic(V) and phosphate capturing in aqueous media, Chem. Eng. J. 331 (2018) 54–63.
[32] M.R. Awual, M.M. Hasan, A.M. Asiri, M.M. Rahman, Cleaning the arsenic(V)

contaminated water for safe-guarding the public health using novel composite material, Composites Part B-Engineering 171 (2019) 294–301.
[33] L. Yohai, H. Giraldo Mejia, R. Procaccini, S. Pellice, K.L. Kunjali, J. Dutta, A. Uheida, Nanocomposite functionalized membranes based on silica nanoparticles cross-linked to electrospun nanofibrous support for arsenic(v) adsorption from contaminated underground water, RSC Advances 9 (2019) 8280–8289.
[34] Y. Wei, S. Wei, C. Liu, T. Chen, Y. Tang, J. Ma, K. Yin, S. Luo, Efficient removal of arsenic from groundwater using iron oxide nanoneedle array-decorated biochar fibers with high Fe utilization and fast adsorption kinetics, Water Res. 167 (2019).
[35] A. Aboelmagd, S.A. El-Safty, M.A. Shenashen, E.A. Elshehy, M. Khairy, M. Sakaic, H. Yamaguchi, Nanomembrane canister architectures for the visualization and filtration of oxyanion toxins with one-step processing, Chem. Asian J. 10 (2015) 2467–2478.
[36] S.A. El-Safty, M. Khairy, M.A. Shenashen, E. Elshehy, W. Warkocki, M. Sakai, Optical mesoscopic membrane sensor layouts for water-free and blood-free toxicants, Nano Res. 8 (2015) 3150–3163.
[37] W. Warkocki, S.A. El-Safty, M.A. Shenashen, E. Elshehy, H. Yamaguchi, N. Akhtar, Photo-induced recovery, optical detection, and separation of noxious SeO_3^{2} using a mesoporous nanotube hybrid membrane, J. Mater. Chem. A 3 (2015) 17578–17589.
[38] A.M. Yousif, O.F. Zaid, I.A. Ibrahim, Fast and selective adsorption of As(V) on prepared modified cellulose containing Cu(II) moieties, Arabian J. Chem. 9 (2016) 607–615.
[39] L. Dambies, E. Guibal, A. Roze, Arsenic(V) sorption on molybdate-impregnated chitosan beads, Colloids Surf A 170 (2000) 19–31.
[40] L. Dambies, T. Vincent, E. Guibal, Treatment of arsenic-containing solutions using chitosan derivatives: uptake mechanism and sorption performances, Water Res. 36 (2002) 3699–3710.
[41] S. Budhi, C. Mukarakate, K. Iisa, S. Pylypenko, P.N. Ciesielski, M.M. Yung, B.S. Donohoe, R. Katahira, M.R. Nimlos, B.G. Trewyn, Molybdenum incorporated mesoporous silica catalyst for production of biofuels and value-added chemicals via catalytic fast pyrolysis, Green Chem. 17 (2015) 3035–3046.
[42] S.A. El-Safty, Organic-inorganic hybrid mesoporous monoliths for selective discrimination and sensitive removal of toxic mercury ions, J. Mater. Sci. 44 (2009) 6764–6774.
[43] A.M. Farnet, L. Qasemian, D. Guiral, E. Ferre, A modified method based on arsenomolybdate complex to quantify cellulase activities: application to litters, Pedobiologia 53 (2010) 159–160.
[44] M. Feng, Y.W. Cui, J.P. Xia, X.T. Zhou, Determination of arsenic in tin smelting slag by the molybdoantimony arsenate blue spectrophotometric method, Appl. Mechn. Mater. 448–453 (2014) 150–153.
[45] F. Li, A. Stein, Functional composite membranes based on mesoporous silica spheres in a hierarchically porous matrix, Chem. Mater. 22 (2010) 3790–3797.
[46] V. Vaiano, G. Iervolino, D. Sannino, L. Rizzo, G. Sarno, A. Farina, Enhanced photocatalytic oxidation of arsenite to arsenate in water solutions by a new catalyst based on MoO_x supported on TiO_2, Appl. Catal., B 160 (2014) 247–253.
[47] R.K. Dhar, Y. Zheng, J. Rubenstone, A. van Geen, A rapid colorimetric method for measuring arsenic concentrations in groundwater, Anal. Chim. Acta 526 (2004) 203–209.
[48] A.K. Pettersson, B. Karlberg, Simultaneous determination of orthophosphate and arsenate based on multi-way spectroscopic-kinetic data evaluation, Anal. Chim. Acta 354 (1997) 241–248.
[49] A.M. Abdel-Lateef, R.A. Mohamed, H.H. Mahmoud, Determination of arsenic(III) and (V) species in some environmental samples by atomic absorption spectrometry, Adv. Chem. Sci. 2 (2013) 110–113.
[50] G. Hanrahan, T.K. Fan, M. Kantor, K. Clark, S. Cardenas, D.W. Guillaume, C.S. Khachikian, Design and development of an automated flow injection instrument for the determination of arsenic species in natural waters, Rev. Sci. Instrum. 80 (2009).
[51] A.D. Idowu, P.K. Dasgupta, Liquid chromatographic arsenic speciation with gas-phase chemiluminescence detection, Anal. Chem. 79 (2007) 9197–9204.
[52] H. Kaur, R. Kumar, J.N. Babu, S. Mittal, Advances in arsenic biosensor development – a comprehensive review, Biosens. Bioelectron. 63 (2015) 533–545.
[53] M.K. Sengupta, P.K. Dasgupta, An automated hydride generation interface to ICPMS for measuring total arsenic in environmental samples, Anal. Chem. 81 (2009) 9737–9743.
[54] H. Shen, P.K. Dasgupta, Electrochemical arsine generators for arsenic determination, Anal. Chem. 86 (2014) 7705–7711.
[55] Y. Song, G.M. Swain, Total inorganic arsenic detection in real water samples using anodic stripping voltammetry and a gold-coated diamond thin-film electrode, Anal. Chim. Acta 593 (2007) 7–12.
[56] A.M. Yousif, A.A. Atia, O.F. Zaid, I.A. Ibrahim, Efficient and fast adsorption of phosphates and sulphates on prepared modified cellulose, J. Dispersion Sci. Technol. 36 (2015) 1628–1638.
[57] J. Das, P. Sarkar, A new dipstick colorimetric sensor for detection of arsenate in drinking water, Environ. Sci. Water Res. Technol. 2 (2016) 693–704.
[58] P.M. Arnal, C. Weidenthaler, F. Schuth, Highly monodisperse zirconia-coated silica spheres and zirconia/silica hollow spheres with remarkable textural properties, Chem. Mater. 18 (2006) 2733–2739.
[59] C. Zhang, D.J. Sun, M. Shen, H.L. Liao, Deposition of hollow sphere In2O3 coatings by liquid flame spray, Surface Engineering.
[60] M. Khoeini, A. Najafi, H. Rastegar, M. Amani, Improvement of hollow mesoporous silica nanoparticles synthesis by hard-templating method via CTAB surfactant, Ceram. Int. 45 (2019) 12700–12707.
[61] M.S.H. Hashemi, F. Eslami, R. Karimzadeh, Organic contaminants removal from industrial wastewater by CTAB treated synthetic zeolite Y, J. Environ. Manage. 233 (2019) 785–792.
[62] H.Y. Kim, Y. Cho, S.W. Kang, Porous cellulose acetate membranes prepared by water pressure-assisted process for water-treatment, J. Ind. Eng. Chem. 78 (2019) 421–424.
[63] S. El-Sherbiny, N.M. Ahmed, Enhancing coated paper mechanical properties via doping kaolin with ammonium molybdate, J. Coat. Technol. Res. 15 (2018) 1379–1390.
[64] R.M. Silverstein, F.X. Webster, D.J. Kiemle, Spectrometric Identification of Organic Compounds, seventh ed., John Wiley & Sons, New York, NY, USA, 2005, p. 512.
[65] W.A. El-Said, M.E. El-Khouly, M.H. Ali, R.T. Rashad, E.A. Elshehy, A.S. Al-Bogami, Synthesis of mesoporous silica-polymer composite for the chloridazon pesticide removal from aqueous media, J. Environ. Chem. Eng. 6 (2018) 2214–2221.
[66] M. Najafi, M. Sadeghi, A. Bolverdi, M.P. Chenar, M. Pakizeh, Gas permeation properties of cellulose acetate/silica nanocomposite membrane, Adv. Polym. Technol. 37 (2018) 2043–2052.
[67] G. Mendes, M. Faria, A. Carvalho, M.C. Goncalves, M.N. de Pinho, Structure of water in hybrid cellulose acetate-silica ultrafiltration membranes and permeation properties, Carbohydr. Polym. 189 (2018) 342–351.
[68] A.E.-A.A. Said, M.M.M.A. El-Wahab, A.M. Alian, Selective oxidation of methanol to formaldehyde over active molybdenum oxide supported on hydroxyapatite catalysts, Catal. Lett. 146 (2016) 82–90.
[69] N.A. Dhas, A. Gedanken, Characterization of sonochemically prepared unsupported and silica-supported nanostructured pentavalent molybdenum oxide, J. Phys. Chem. B 101 (1997) 9495–9503.
[70] B. An, T.R. Steinwinder, D.Y. Zhao, Selective removal of arsenate from drinking water using a polymeric ligand exchanger, Water Res. 39 (2005) 4993–5004.
[71] R.-M. Couture, P. Van Cappellen, Reassessing the role of sulfur geochemistry on arsenic speciation in reducing environments, J. Hazard. Mater. 189 (2011) 647–652.
[72] M.M. Ghosh, J.R. Yuan, Adsorption of inorganic arsenic and organosenicals on hydrous oxides, Environ. Prog. 6 (1987) 150–157.
[73] S.K. Gupta, K.Y. Chen, Arsenic removal by adsorption, J. Water Pollut. Control Fed. 50 (1978) 493–506.
[74] Z.L. Li, S.F. Mou, Z.M. Ni, J.M. Riviello, Sequential determination of arsenite and arsenate by ion chromatography, Anal. Chim. Acta 307 (1995) 79–87.
[75] K. Morita, E. Kaneko, Spectrophotometric determination of arsenic in water samples based on micro particle formation of ethyl violet-molybdoarsenate, Anal. Sci. 22 (2006) 1085–1089.
[76] K. Toda, T. Ohba, M. Takaki, S. Karthikeyan, S. Hirata, P.K. Dasgupta, Speciation-capable field instrument for the measurement of arsenite and arsenate in water, Anal. Chem. 77 (2005) 4765–4773.
[77] S. Tsang, F. Phu, M.M. Baum, G.A. Poskrebyshev, Determination of phosphate/arsenate by a modified molybdenum blue method and reduction of arsenate by $S_2O_4^{2-}$, Talanta 71 (2007) 1560–1568.
[78] H. Matsunaga, C. Kanno, T.M. Suzuki, Naked-eye detection of trace arsenic(V) in aqueous media using molybdenum-loaded chelating resin having beta-hydroxypropyl-di(β-hydroxyethyl) amino moiety, Talanta 66 (2005) 1287–1293.
[79] M.A. Shenashen, S.A. El-Safty, E.A. Elshehy, Monolithic scaffolds for highly selective ion sensing/removal of Co(II), Cu(II), and Cd(II) ions in water, Analyst 139 (2014) 6393–6405.
[80] S. Lagergren, About the theory of so-called adsorption of soluble substances, Kungliga Svenska Vetenskapsakademiens 24 (1898) 1–39.
[81] Y.S. Ho, G. McKay, Pseudo-second order model for sorption processes, Process Biochem. 34 (1999) 451–465.
[82] C. Tien, Adsorption Calculations and Modeling, Butterworth-Heinemann, Newton, MA, 1994, p. 243.
[83] T. Pick, Assessing Water Quality for Human Consumption, Agriculture, and Aquatic Life Uses, in: USDA (Ed.) Environmental Technical Notes, National Resources Conservation Service – US Department of Agriculture, Montana (USA), 2011, pp. 31.
[84] H. Jeong, H. Kim, T. Jang, Irrigation water quality standards for indirect wastewater reuse in agriculture: a contribution toward sustainable wastewater reuse in South Korea, Water 8 (2016) art. 169.
[85] S.A. El-Safty, M.A. Shenashen, M. Ismael, M. Khairy, M.R. Awual, Optical mesosensors for monitoring and removal of ultra-trace concentration of Zn(II) and Cu(II) ions from water, Analyst 137 (2012) 5278–5290.
[86] V.S. Saji, C.W. Lee, Molybdenum, molybdenum oxides, and their electrochemistry, ChemSusChem 5 (2012) 1146–1161.
[87] K. Gupta, U.C. Ghosh, Arsenic removal using hydrous nanostructure iron(III)-titanium(IV) binary mixed oxide from aqueous solution, J. Hazard. Mater. 161 (2009) 884–892.
[88] G.-S. Zhang, J.-H. Qu, H.-J. Liu, R.-P. Liu, G.-T. Li, Removal mechanism of As(III) by a novel Fe-Mn binary oxide adsorbent: oxidation and sorption, Environ. Sci. Technol. 41 (2007) 4613–4619.
[89] G. Zhang, Z. Ren, X. Zhang, J. Chen, Nanostructured iron(III)-copper(II) binary oxide: a novel adsorbent for enhanced arsenic removal from aqueous solutions, Water Res. 47 (2013) 4022–4031.
[90] C.A. Martinson, K.J. Reddy, Adsorption of arsenic(III) and arsenic(V) by cupric oxide nanoparticles, J. Colloid Interface Sci. 336 (2009) 406–411.
[91] J. Hlavay, K. Polyak, Determination of surface properties of iron hydroxide-coated alumina adsorbent prepared for removal of arsenic from drinking water, J. Colloid Interface Sci. 284 (2005) 71–77.
[92] Z. Ren, G. Zhang, J.P. Chen, Adsorptive removal of arsenic from water by an iron-zirconium binary oxide adsorbent, J. Colloid Interface Sci. 358 (2011) 230–237.
[93] K.Z. Elwakeel, Removal of arsenate from aqueous media by magnetic chitosan resin immobilized with molybdate oxoanions, Int. J. Environ. Sci. Technol. 11 (2014)

1051–1062.
[94] K.B. Payne, T.M. Abel-Fattah, Adsorption of arsenate and arsenite by iron-treated activated carbon and zeolites: effects of pH, temperature, and ionic strength, J. Environ. Sci. Health., Part A Environ. Sci. Eng. Toxic Hazard. Subst Control 40 (2005) 723–749.
[95] J.S. Markovski, D.D. Markovic, V.R. Dokic, M. Mitric, M.D. Ristic, A.E. Onjia, A.D. Marinkovic, Arsenate adsorption on waste eggshell modified by goethite, α-MnO_2 and goethite/α-MnO_2, Chem. Eng. J. 237 (2014) 430–442.
[96] R.N. Shinde, A.K. Pandey, R. Acharya, R. Guin, S.K. Das, N.S. Rajurkar, P.K. Pujari, Chitosan-transition metal ions complexes for selective arsenic(V) preconcentration, Water Res. 47 (2013) 3497–3506.
[97] D. Tiwari, S.M. Lee, Novel hybrid materials in the remediation of ground waters contaminated with As(III) and As(V), Chem. Eng. J. 204 (2012) 23–31.